Origin of the Lunar Ultramafic Glasses Constrained by Experiments and Models

by

Megan E. Guenther

S. B. Earth, Atmospheric and Planetary Science
Massachusetts Institute of Technology, 2021

SUBMITTED TO THE DEPARTMENT OF EARTH, ATMOSPHERIC AND PLANETARY SCIENCES IN PARTIAL FULFILLMENT OF THE REQUIREMENTS FOR THE DEGREE OF

MASTER OF SCIENCE IN EARTH AND PLANETARY SCIENCES
AT THE
MASSACHUSETTS INSTITUTE OF TECHNOLOGY

May 2022

Signature of Author: _____
Department of Earth, Atmospheric and Planetary Sciences
May 6, 2022

Certified by: _____
Timothy L. Grove
Robert R. Shrock Professor of Earth and Planetary Sciences
Thesis Supervisor

Accepted by _____
Robert Van der Hilst
Department Head

Origin of the Lunar Ultramafic Glasses Constrained by Experiments and Models

by

Megan E. Guenther

Submitted to the Department of Earth, Atmospheric and Planetary Sciences
on May 6, 2022, in partial fulfillment of the
requirements for the degree of
Master of Science in Earth and Planetary Sciences

ABSTRACT

To place further constraints on the origin of the lunar ultramafic glasses and the evolution of the lunar interior, phase equilibrium experiments are carried out on two synthetic compositions which represent hybridized, bulk source compositions of (1) high-titanium and (2) very low-titanium/high-aluminum primary magmas. The compositions are designed to produce liquids compositionally similar to the high-Ti Apollo 14 Black (A14B) glass (16.4 wt.% TiO_2) and the high-Al Apollo 14 Very Low Titanium (A14VLT) glass (0.61 wt.% TiO_2, 9.60 wt.% Al_2O_3). Experiments on the synthetic source composition "HiTi1" at pressures of 1.5-2.0 GPa, temperatures of 1380-1460°C, and degrees of melting ≈ 30% produce the best fitting melts to A14B. Experiments on the synthetic source composition "VLTCum1" at pressures of 1.8-2.0 GPa, temperatures of 1460-1480°C, and degrees of melting ≈ 30-45% produce the best fitting melts to A14VLT. The forward melting experiments performed on both source compositions contain equilibrium mineral assemblages that match those obtained through inverse melting experiments on the glass compositions. Experimental conditions that produced good fits to the target glass compositions overlap with conditions corresponding to previously determined olivine-orthopyroxene multiple saturation pressures and temperatures for the glasses. Our experimental results confirm melting from a compositionally heterogeneous lunar mantle source that was hybridized through cumulate mantle overturn. Using a petrogenetic mass balance model, we suggest source components which could have been involved in the production of these hybridized source regions. We also calculate density as a function of pressure for several high-Ti glasses as well as the A14VLT glass and determine if these liquids are positively buoyant at their hypothesized depth of origin relative to their mantle residue. We find that the A14VLT glass is always positively buoyant at relevant depths, while some of the high-Ti glasses are positively buoyant only at depths corresponding to more oxidizing source region compositions.

Thesis Supervisor: Timothy L. Grove

Title: Robert R. Shrock Professor of Earth and Planetary Sciences

Acknowledgements

I would like to first and foremost thank my advisor, Timothy Grove, for all his encouragement, help, and support over the past five years. Since my very first days as a freshman on the Yellowstone pre-orientation trip to presenting my research at LPSC for the fourth time this year, Tim has inspired and challenged me to grow as a scientist and person. I could not have made it this far without the invaluable opportunities Tim has given me, and I am so grateful.

I extend my gratitude to my thesis committee, Oliver Jagoutz and Matej Pej, for their valuable time and input. I would like to especially thank Oli for supporting me throughout my time at MIT and extending me the opportunity to TA for his classes. I have grown so much as a teacher and mentor through these experiences. Thank you so much to all the students I have had over the years. You have made teaching such a joy for me.

I would also like to thank Stephanie Krein for her guidance and expertise through my undergrad and grad careers and Nilanjan Chatterjee for gracious help with the MIT Microprobe. To everyone else in the Grove lab—Mira, Patrick, Susana—you have made my experience here all the better. To my parents, I love you so much. Thank you for your unconditional support and encouragement. Finally, I want to send love and thanks to everyone who has supported me through the ups and downs of MIT and cheered me on through everything.

Table of Contents

1. Introduction

The volcanic mare glasses collected during the Apollo missions (1969-1972) provide a unique view of the chemical and physical structure of the lunar interior. These small glass beads, found in collected lunar regolith samples, formed in volatile assisted, high-temperature fire fountain eruptions. They are extremely ultramafic, with a combined MgO + FeO of 35 to 40 wt.%, making them ideal candidates for experimental study of melt generation (Delano, 1986).

The lunar ultramafic glasses also exhibit significant compositional variability. Delano (1986) has divided the glasses into 25 distinct suites. Variability is especially apparent in TiO_2 content, which ranges from 0.2 to 16.4 wt.% between the ultramafic glass suites (Figure 1). The suites cluster into distinct groups of TiO_2 content, which also correlates with glass color (green (<3 wt. %), yellow (3-7 wt.%), orange (8-11 wt.%), red (13-14 wt.%), black (15.5-17 wt.%)). As noted in Figure 1, there is also compositional variability within the suites themselves. The Apollo 14 black glass (A14B) suite, for example, has Mg #'s (Mg # = molar [Mg/ (Mg + Fe)]) that vary from 0.47 to 0.53.

The goal of investigating these glasses is to determine the source regions that produced them and the possible processes which can explain both their between- and within-suite chemical trends. Understanding the genesis of these magmas is important because the processes that produced their variability can provide significant information on the thermal conditions and chemical and physical structure of the Moon's interior during the solidification of the lunar magma ocean (4.5-4.3 Ga), lunar mantle overturn (~4.3 Ga (Sio et al., 2020)), and the later remelting and eruption of the glasses (3.7-3.3 Ga (Husain and Schaeffer, 1973; Spangler et al., 1984)).

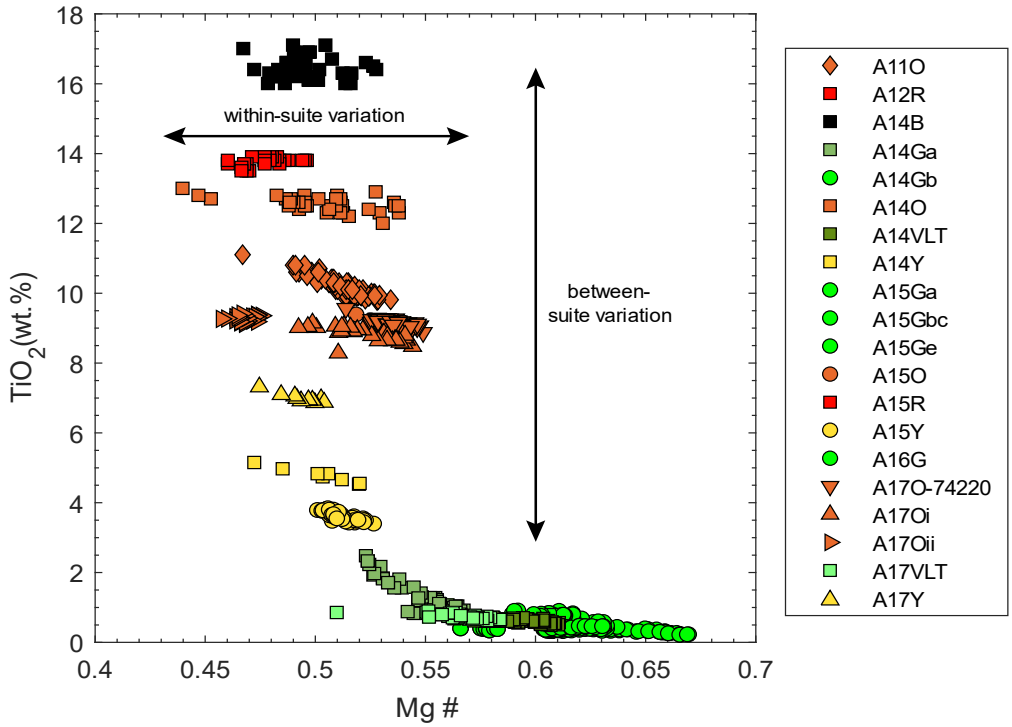

Figure 1. Between- and within-suite variation in TiO_2 and Mg# (Mg# = molar Mg/ (Mg + Fe)) demonstrated among a selection of the lunar glass suites. Glass data from Delano (1986).

This study will focus on elucidating the processes involved in the production of the source regions and that produced the primary magmas of the high-titanium A14B glass and the very low-titanium (VLT) glass from the Apollo 14 mission (A14VLT). To test the hypothesis that these glasses are produced from a hybridized source region, forward melting experiments are performed on calculated source compositions for each of the glasses. A petrologic model is then utilized to provide possible explanations for the genesis of theses source regions through hybridization or other means.

1.1 Early lunar evolution – differentiation and lunar mantle overturn

Determining the origin of the lunar ultramafic glasses begins with understanding the processes that occurred within the lunar mantle prior to their melting and subsequent

eruption. Since the first samples collected from the Apollo missions were analyzed, evidence from the chemical composition and mineralogical make-up of basalts and soils has pointed to the early moon experiencing a profound chemical differentiation event caused by the crystallization of a lunar magma ocean (LMO). Early investigators noted that Apollo 11 soil samples from older highlands terrain comprised of Ca- and Al-rich plagioclase feldspar (Smith et al., 1970; Wood et al., 1970). Unusual and distinct major and trace element signatures were also noted in lunar samples, particularly negative Europium anomalies in mare basalts and corresponding positive anomalies in the highlands anorthosite (e.g., Philpotts and Schnetzler, 1970; Taylor, 1973). These observations, among others, led to the hypothesis that the moon had experienced an early differentiation event where plagioclase, olivine, and pyroxenes were crystallizing together from the LMO and the buoyant plagioclase separated from the magma and cumulate pile by floating to form an early anorthosite crust (e.g., Smith et al., 1970; Wood et al., 1970; Taylor and Jakes, 1974).

Subsequent work has attempted to determine the crystallization sequence of the LMO using experiments and models (e.g., Snyder et al., 1992; Elkins-Tanton et al., 2011; Elardo et al., 2011; Lin et al., 2017; Charlier et al., 2018). The results vary according to the initial extent of melting, depth of the magma ocean, whole moon composition, and other inferred parameters utilized in the models. Nonetheless, many petrologic models of LMO solidification are broadly similar. They predict that the first phase to crystallize is olivine, followed by low-calcium pyroxene. Much further in the crystallization process (>70% solidification) anorthitic plagioclase and clinopyroxene solidify (Snyder et al., 1992; Elkins-Tanton et al., 2011; Lin et al., 2017; Charlier et al., 2018). Near the very end of

LMO solidification (>90% solidification), ilmenite becomes a liquidus phase with plagioclase and clinopyroxene (e.g., Snyder et al., 1992; Elkins-Tanton et al., 2011; Charlier et al., 2018). This ilmenite crystallization would occur at depths of 100-150km (Hess and Parmentier, 1995; Van Orman and Grove, 2000). The late stage cumulates are enriched in TiO_2, FeO, and KREEP (K, Rare Earth Elements, and Phosphorus) components and are thus denser than the underlying mantle cumulates (e.g., Snyder et al., 1992; Hess and Parmentier, 1995; Charlier, 2018). The natural result of this unstable configuration is thought to be lunar cumulate mantle overturn, whereby the pristine cumulates are redistributed by solid-state mantle flow and the dense, Ti-rich cumulates descend much deeper into the lunar mantle (Ringwood and Kesson, 1976; Hess and Parmentier, 1995). Several models based on the physical and chemical properties of the lunar mantle have investigated and predicted overturn of the magma ocean cumulate pile (e.g., Herbert, 1980; Hess and Parmentier, 1995, Elkins-Tanton, 2011; Yu et al., 2019; Zhao et al., 2019). Many studies have invoked lunar mantle overturn to explain the high-Ti lunar volcanic rocks and glasses, as well to explain other observations including asymmetrical KREEP concentrations (e.g., Delano, 1986; Parmentier et al., 2002; Shearer et al., 2006; Krawczynski and Grove, 2012).

1.2. Previous hypotheses for lunar glass petrogenesis

The lunar ultramafic glasses were initially believed to be remelts of the pristine LMO cumulates. The low-Ti magmas were attributed to partial melting of the early olivine + orthopyroxene cumulates at significant depths, while the high-Ti magmas were initially proposed to be remelts of the shallow, Ti-rich cumulates that were the last to crystallize from the LMO (Taylor and Jakes, 1974; Walker et al., 1975). However, that idea would

prove to be inconsistent with experimental studies on the ultramafic glasses. Phase equilibrium experiments predict depths of melting at similar and significant depths (>250 km) for both the high- and low-Ti glasses, based on the multiple saturation of olivine and orthopyroxene on the liquidus of these glass compositions at high pressures (Figure 2).

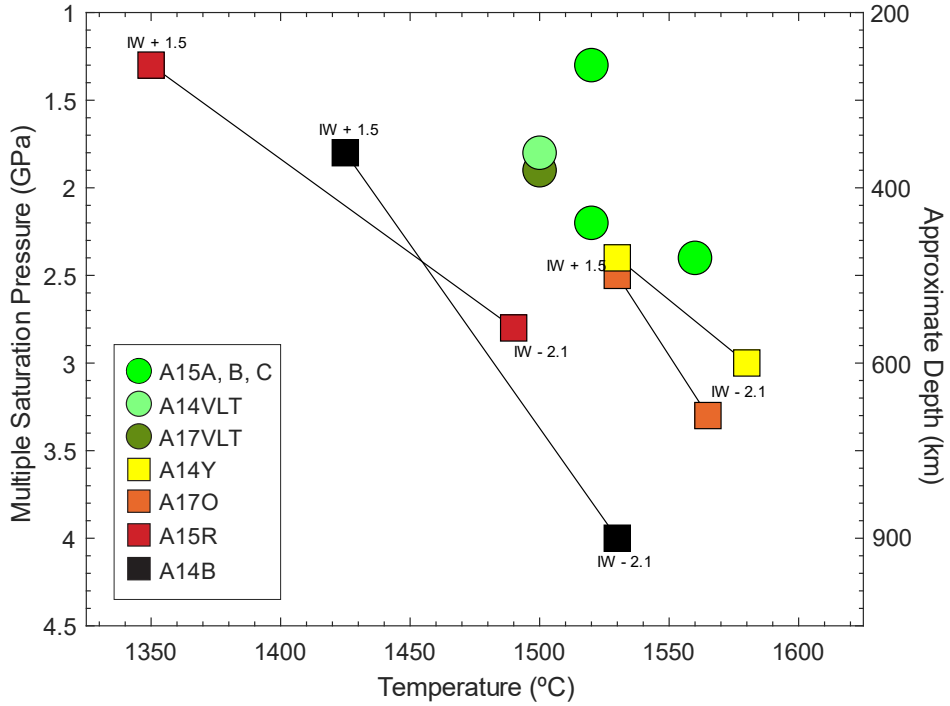

Figure 2. Pressure and temperatures of olivine-orthopyroxene multiple saturation obtained from experimental investigation of lunar glasses which span a range of TiO_2 contents (0.2-16.4 wt.%) (Chen et al., 1972; Wagner and Grove, 1997; Elkins-Tanton et al., 2003; Krawczynski and Grove, 2012; Brown and Grove, 2015; Guenther, 2021). Circles represent compositions with 0.2-1.0 wt. % TiO_2, and square represent compositions with 4-17 wt. % TiO_2. Experimental oxygen fugacity conditions are noted for the high-Ti compositions, as it influences multiple saturation pressure and temperature.

Thus, others have hypothesized that the high-Ti magmas could be the product of assimilation of the late-stage ilmenite bearing cumulates at shallow depths by a low-Ti magma that melted deeper in the mantle (e.g., Hubbard and Minear, 1975; Wagner and

Grove, 1997). However, the shallow assimilation model of Hubbard and Minear (1975) was rejected by Ringwood and Kesson (1976) based on heat-budget constraints and compositional ratios. To reconcile these constraints with the experimental evidence of depths of melting, Ringwood and Kesson (1976) proposed the idea of hybridization via lunar mantle overturn, where the dense, ilmenite bearing cumulates sank into the lunar interior, mixing the high- and low-Ti components of the cumulate pile and creating hybridized source compositions which would later remelt and could produce a wide range of magma compositions. Several subsequent studies have supported the hybridization hypothesis (Hess and Parmentier, 1995; Van Orman and Grove, 2000; Singletary and Grove, 2008; Kommescher et al., 2020).

Singletary and Grove (2008) performed experiments on a model hybridized source composition to assess whether a hybridized cumulate source could produce the high-Ti glasses. Their Magma Ocean Cumulate Hybrid (MOCH) composition was designed by combining a deep olivine + orthopyroxene cumulate inferred from the differentiation model of Hess and Parmentier (1995), a late stage high-Ti model cumulates (Snyder et al., 1992), and a small amount of a KREEP component (Warren and Wasson, 1979). The MOCH source composition can produce glasses with moderate (~9.0 wt. %) TiO_2 contents like those of the Apollo 17 Orange (A17O) glass, but it cannot produce glasses with TiO_2 contents greater than 10 wt. % TiO_2, such as A14B.

Other models (Shearer et al., 1996; Elkins-Tanton et al., 2003; Barr and Grove, 2013; Brown and Grove, 2015) suggest the mixing of magmas produced from two or more source regions to explain the between- and/or within-suite variation in the lunar ultramafic glasses. The distinction between the magma mixing and hybridization models is that

magma mixing involves liquids from different sources mixing in various proportions and at potentially different pressures, which could make the inferred depths of melting obtained from multiple saturation experiments on the erupted glass inaccurate. Hybridization, however, would involve the mixing of different cumulate materials at a given depth with later remelting, which would produce one melting trend and preserve the multiple saturation pressure as an accurate depth of melting.

While mixing is a possible explanation of the compositional variability demonstrated by the glasses, most models involving magma mixing cannot adequately explain all of the variation seen. Several studies have concluded that shallow assimilation or mixing of partial melts of ilmenite bearing cumulates by ascending low-Ti melts from lunar mantle cannot be invoked to explain the formation of high-Ti lunar magmas. Van Orman and Grove (2000) determined that compositional constraints exclude assimilation as a viable mechanism to produce the high-Ti glasses. Furthermore, Brown et al. (2021) concluded that the mixing of melts of pristine, late-stage Fe-Ti cumulates with other melts of LMO cumulate components from varying depths in the lunar mantle cannot account for the production of the high-Ti glass suites.

1.3 Motivation for this study

Brown et al. (2021) identified three major and distinct groups of primary magmas which are responsible for the lunar ultramafic glass suites: high-Ti, low-Al, and high-Al (Figure A). These would have derived from compositionally distinct source regions, which explains the broad, between suite-variability demonstrated by the glasses. Secondary modification may have occurred (i.e., olivine fractionation, mixing, assimilation, reaction)

to explain the between suite chemical trends. These secondary modifications can be identified and decoupled from the primary compositional trends. In identifying primary magmas, their pressures and temperatures of melt generation and residual source mineralogy can be determined and aid in discerning the primary processes that generated their source regions.

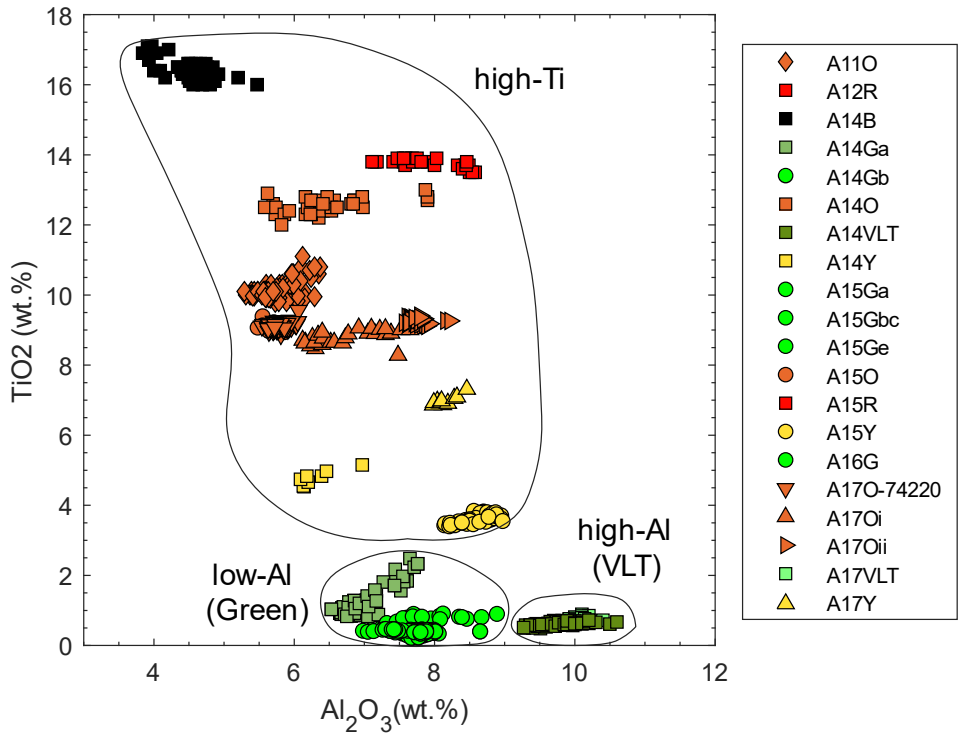

Figure 1. Compositional variation in TiO_2 and Al_2O_3. Primary magma groups are indicated, as identified by Brown et al. (2021).

Motivated by the need to further explore the feasibility of hybridization of LMO cumulates as a mechanism for generating the source regions of the lunar ultramafic glass primary magmas as well as the inability of current models to adequately account for the origin of the highest TiO_2 glasses, we design and perform experiments on two source compositions: High-Titanium-1 (HiTi1) and Very-Low-Titanium-Cumulate-1

(VLTCum1). Rather than inferring cumulate compositions and proportions (i.e., Singletary and Grove, 2008), we use the compositional information from an erupted high-Ti glass of the A14B suite (high-Ti primary magma) and very low-Ti glass of the A14VLT suite (high-Al primary magma) to calculate a bulk source composition. We then use a petrogenetic model to assess if hybridization is a reasonable mechanism, and if so, which cumulates and in what proportions could have hybridized to create their primary magma sources. In this way, we can place better constraints on the redistribution and hybridization of cumulates in the lunar interior.

2. Methods

2.1 Starting materials

Hybridized cumulate compositions designed to produce a liquid similar to a primary magma component of the high-titanium A14B glass and the low-titanium, high-aluminum 14-VLT glass were calculated using the batch melting equation (Equation (1)) and were then used as starting materials for the experiments in the Massachusetts Institute of Technology experimental petrology laboratory.

$$C_{source} = D \times C_{melt}(1 - F) + C_{melt} \times F \quad (1)$$

2.1.1 Calculating the A14B hybridized source: HiTi1

To calculate a viable starting material, named HiTi1, we use Eq. 1 to solve for each element in an erupted A14B glass (C_{melt}), the composition of which is shown in Table 1. This composition was selected because it is the most primary found within the A14B suite. A 30% degree of melting (F) is assumed, because this is the approximate degree of melting for when a spinel phase would disappear, corresponding with a maximum in TiO_2 content. Mineral/melt partition coefficients (D) from A14B multiple saturation experiments (60% opx, 40% oliv) (Wagner & Grove, 1997; Guenther, 2021) are used to calculate a bulk D utilized in Eq. 1. The calculated HiTi1 composition (C_{source}) is shown in Table 2.

2.1.2 Calculating the A14VLT hybridized source: VLTCum1

The erupted A14VLT glass composition (C_{melt}) used for calculations of starting composition VLTCum1 is shown in Table 1. The procedure for calculations with Equation (1) is the same as described in the previous section. Ds were obtained from a multiply

saturated experiment of Chen et al. (1982), and a bulk D was calculated using the proportions 50% opx and 50% oliv. The calculated VLTCum1 (C_{source}) is shown in Table 2.

2.1.3 Preparing experimental starting materials

The starting hybridized source compositions HiTi1 and VLTCum1 were prepared by grinding and mixing high purity reagent grade oxides and silicates (SiO_2, TiO_2, Al_2O_3, Fe_2O_3, MnO, MgO, $CaSiO_3$, Na_2SiO_3, K_2CO_3, Cr_2O_3) in an agate mortar under ethanol for 6 hours. To obtain an overall stoichiometry of FeO, Fe_2O_3 was added to the initial mixtures, and Fe-metal sponge was added for the last 45 minutes of grinding. The mixed powder was then pressed into pellets with Elvanol as a binding agent. The pellets were hung on a 0.004 Pt wire in a Deltech vertical gas mixing furnace. They were conditioned at 1-atm and 1000 °C under oxygen fugacity conditions near the QFM buffer for 48 hours using a flow of CO_2 and H_2 gases.

2.2 Experimental techniques

High pressure, high temperature experiments were performed with a ½" piston cylinder device (Boyd and England, 1960). The ground and conditioned starting material was packed into a graphite capsule. Packed capsules along with porous MgO spacers were dried at 120°C in a desiccated drying oven for at least 24 hours prior to running an experiment. Following the methods of Médard et al. (2008), the capsule was then covered with a graphite lid and placed in a platinum tube which had been triple crimped, welded shut, and flattened on one end. The open end of the Pt tube was then crimped and welded shut to seal

in the graphite capsule. This experimental charge was then placed in a 99.8% dense Al_2O_3 ring and centered in a graphite furnace using the dried MgO spacers. The furnace was placed within a sintered $BaCO_3$ pressure cell for experiments.

Experiments were run at temperatures of 1380-1500°C and pressures of 1.5-2.55 GPa. Pressure was calibrated used the Ca-Tschermak breakdown reaction (Hays, 1966a) and the spinel to garnet transition in the CMAS system (Longhi, 2005a). Pressures are precise to ±50 MPa. Temperature was measured with a W-Re thermocouple without an emf pressure correction. Temperatures are precise to ±10°C.

Médard et al. (2008) determined that the oxygen fugacity imposed on the sample from the graphite capsule is IW + 1.5. For each experiment, the assembly was first pressurized to 1 GPa at room temperature, and then the temperature was raised at a rate of 100°C/min to 865°C. The experiment was held at these conditions for 3 min, then the pressure was increased to the desired value. After 3 additional min at these conditions, the temperature was raised at a rate of 50°C/min until the final run conditions were achieved. Temperatures were maintained to within ±2°C for the duration of the experiment. Experimental durations ranged from 24 to 114 hours.

Experiments were quenched by shutting off the power and releasing pressure simultaneously, in order to minimize quench crystal growth during the cooling of the glass (Putirka et al., 1996a). Run conditions are reported in Tables 3 and 4. Figure 3 shows typical results for HiTi1 and VLTCum1 experiments.

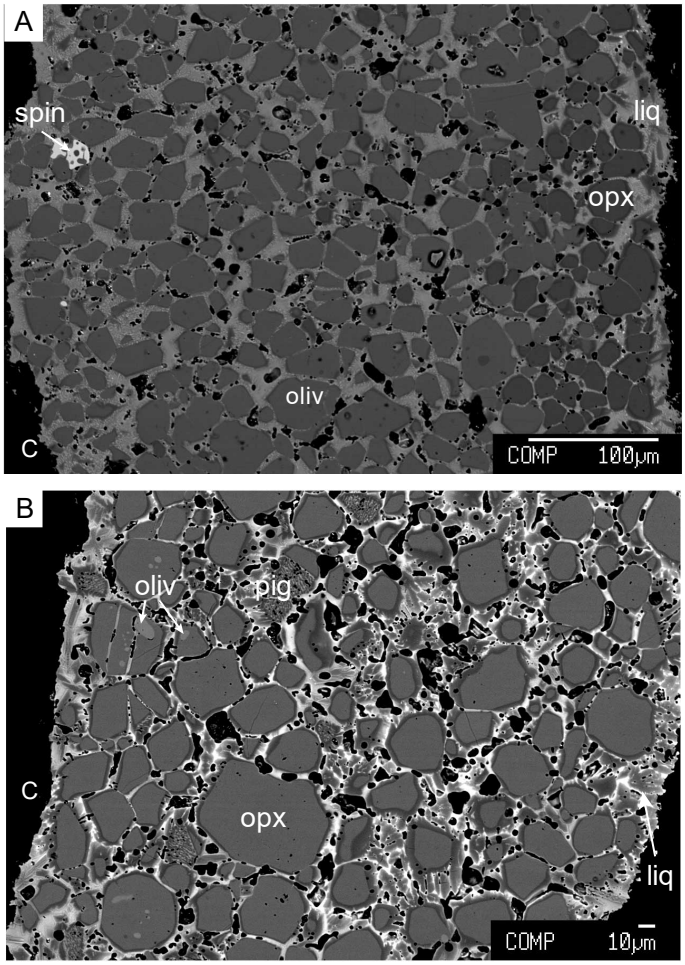

Figure 3. Electron backscattered images of experimental products. (A) HiTi1 experiment D416. Visible are the phases melt, olivine (oliv), orthopyroxene (opx), and spinel (spin) inside the graphite (C) capsule. (B) VLTCum1 experiment C666 with phases liq, oliv, opx, and pigeonite (pig) present in C capsule.

2.3 Analytical methods

Compositions of the glasses and minerals were acquired using wavelength dispersive spectrometry on the JEOL JXA-8200 Superprobe at the electron microprobe facility at MIT. Analyses were performed with a beam current of 10 nA and an accelerating voltage of 15 kV. Glass analyses were performed with a 10 µm diameter defocused beam, and a beam spot size of 1-2 µm was used for mineral analyses. Natural and synthetic standards were used, and the CITZAF correction package of Armstrong (1995). As outlined in

Armstrong (1995), the atomic number correction of Duncumb and Reed, Heinrich's tabulation of absorption coefficients, and the fluorescence correction of Reed were used to obtain a quantitative analysis. Mineral and glass analyses are reported in Tables 5 and 6. Experimental melt compositions were compared to the erupted target compositions by calculating Aitchison distances:

$$\Delta_S(x, X) = \sqrt{\sum_{i=1}^{D} \left\{ \log \frac{x_i}{g(x)} - \log \frac{X_i}{g(X)} \right\}^2} \quad (2)$$

Where g(x) is the geometric mean and $\Delta_S(x, X)$ defines a distance in the simplex sample space between two D-part compositions of x and X (Aitchison et al., 2000). Aitchison distances in this study were calculated using the six major oxides SiO_2, TiO_2, Al_2O_3, FeO, MgO, and CaO and the minor oxides Cr_2O_3 and MnO. Lower Aitchison distances correspond to a smaller overall difference between two compositions. This method was selected because it satisfies the properties of scale invariance, perturbation invariance, permutation invariance, and sub-compositional dominance (Aitchison et al., 2000).

2.4 Petrogenetic model methods

We set up and solve a mass balance problem that models the combination of different endmembers to produce a hybridized cumulate composition. The model utilizes lunar magma ocean cumulates from the LMO crystallization model of Charlier et al. (2018), estimates of KREEP components (Neal and Taylor, 1989; Charlier et al., 2018), primitive lunar mantle melts (Longhi, 2006), and high-Ti cumulate remelts from experiments (Brown and Grove, 2017; Brodsky et al., 2019) as end members and the calculated bulk compositions of HiTi1 and VLTCum1 as target source compositions. We test up to 200,000 hybridized compositions for each model comprised of two to three endmembers calculated

in varying proportions. We then find the end-member compositions and corresponding proportions which minimize the mean compositional distance between the target source composition and the modelled hybridized bulk composition (RMSE < 1).

.

Table 1.
Erupted glass compositions used for calculating experimental source composition.

Composition	SiO_2	TiO_2	Al_2O_3	Cr_2O_3	FeO	MnO	MgO	CaO	Na_2O	K_2O	Total	Mg#
A14B	32.68	16.69	3.99	0.95	24.98	0.32	13.82	6.42	0.07	0.08	100.00	0.50
A14VLT	46.00	0.61	9.60	0.59	18.30	0.23	15.40	9.21	0.08	0.12	100.14	0.60

Table 2.
Calculated synthetic starting compositions used in this study and Singletary and Grove (2008).

Composition	SiO_2	TiO_2	Al_2O_3	Cr_2O_3	FeO	MnO	MgO	CaO	Na_2O	K_2O	Total	Mg#
HiTi1	40.99	5.30	2.08	0.69	18.39	0.68	29.04	2.78	0.03	0.03	100.00	0.74
VLTCum1	50.65	0.20	5.26	0.63	13.12	0.21	24.10	5.77	0.02	0.03	100.00	0.77
MOCH	45.44	4.22	2.64	0.19	18.97	0	23.84	4.6	0	0	99.9	0.69

Table 3
Run conditions and products for HiTi1 starting material.

Run	Capsule	Pressure (GPa)	Temperature (°C)	Time (h)	Phases	% liq	% Fe Loss/Gain	Oliv K_D	Opx K_D
C661	C+Pt	2.6	1500	71	liq+oliv+opx	31.7	-0.2	0.25	0.23
C662	C+Pt	2.5	1480	72.75	liq+oliv+opx	31.8	-0.2	0.28	0.24
C663	C+Pt	2.5	1460	114.3	liq+oliv+opx	33.3	-4.6	0.26	0.24
C655	C+Pt	2.0	1460	47.25	liq+oliv+opx	32.1	-0.6	0.28	0.24
C654	C+Pt	2.0	1440	73	liq+oliv+opx+spin	32.6	-2.2	0.27	0.25
D416	C+Pt	2.0	1420	71.4	liq+oliv+opx+spin	32.1	3.4	0.27	0.23
D414	C+Pt	1.5	1400	73	liq+oliv+opx	33	-0.7	0.30	0.25
C651	C+Pt	1.5	1380	24	liq+oliv+opx+spin	28	7.5	0.32	0.28

Table 4
Run conditions and products for VLTCum1 starting material.

Run	Capsule	Pressure (GPa)	Temperature (°C)	Time (h)	Phases	% liq	% Fe Loss/Gain	Oliv K_D	Opx K_D
C666	C+Pt	2.0	1460	72	liq+oliv+opx+pig	41.3	0.3	0.36	0.33
C665	C+Pt	1.9	1480	71.5	liq+opx	30.1	-7.3		0.33
C667	C+Pt	1.8	1480	72	liq+oliv+opx	44.6	-0.1	0.37	0.32

Table 5

Electron microprobe analyses of HiTi1 experiments in oxide weight percents and their 1-σ errors from replicate analyses.

Run	Phase	n	SiO_2	1-σ	TiO_2	1-σ	Al_2O_3	1-σ	Cr_2O_3	1-σ	FeO	1-σ	MnO	1-σ	MgO	1-σ	CaO	1-σ	Na_2O	1-σ	K_2O	1-σ	Total
C651	liq	15	33.43	1.90	18.72	1.68	5.21	0.37	0.90	0.26	19.97	0.85	0.37	0.02	12.95	1.85	7.97	1.19	0.15	0.08	0.02	0.02	99.69
	oliv	7	38.03	0.17	0.21	0.02	0.08	0.01	0.33	0.02	19.95	0.11	0.60	0.01	40.79	0.12	0.25	0.02					100.23
	opx	10	53.11	0.29	1.17	0.04	1.79	0.10	0.89	0.04	12.09	0.08	0.25	0.02	28.50	0.14	1.52	0.05	0.03	0.02	0.01	0.00	99.37
	spin	10	0.63	0.52	14.00	0.27	9.92	0.25	34.30	0.75	28.58	0.21	0.73	0.04	11.36	0.33	0.13	0.14	0.00	0.01	0.03	0.02	99.69
C654	liq	11	35.33	0.98	16.01	0.52	5.07	0.12	0.80	0.04	20.98	0.30	0.85	0.02	12.40	0.40	7.14	0.19	0.19	0.05	0.05	0.01	98.81
	oliv	20	38.50	0.16	0.11	0.03	0.07	0.02	0.29	0.02	19.10	0.25	0.61	0.02	41.11	0.24	0.22	0.01					100.00
	opx	10	53.23	0.70	0.91	0.14	1.95	0.28	1.04	0.16	11.90	0.66	0.34	0.15	28.13	0.60	1.51	0.18	0.01	0.02	0.00	0.00	99.02
	spin	6	4.89	3.28	10.26	0.81	9.57	0.43	33.95	1.73	26.49	0.95	0.71	0.02	13.65	0.93	0.21	0.14	0.03	0.04	0.03	0.03	99.78
C655	liq	28	34.57	0.20	15.83	0.10	4.86	0.09	0.87	0.04	21.75	0.22	0.58	0.24	13.01	0.24	7.31	0.12	0.17	0.05	0.05	0.01	98.99
	oliv	17	38.77	0.21	0.15	0.03	0.07	0.01	0.31	0.02	19.38	0.12	0.60	0.03	41.21	0.23	0.21	0.02					100.71
	opx	8	53.65	0.11	0.93	0.05	1.74	0.08	0.96	0.05	11.67	0.15	0.23	0.01	29.08	0.22	1.45	0.03	0.01	0.02	0.00	0.00	99.72
C661	liq	14	34.10	0.74	16.29	0.21	4.93	0.21	0.89	0.04	22.90	0.23	0.86	0.03	12.55	0.60	7.52	0.23	0.13	0.04	0.04	0.01	100.20
	oliv	17	38.56	0.16	0.14	0.02	0.08	0.01	0.27	0.02	19.24	0.17	0.61	0.02	41.67	0.25	0.21	0.01					100.79
	opx	14	54.15	0.27	0.86	0.04	2.15	0.09	0.94	0.04	11.70	0.17	0.55	0.02	28.35	0.39	1.60	0.03	0.03	0.03	0.00	0.01	100.33
C662	liq	11	35.59	2.33	16.42	1.85	5.34	1.07	0.77	0.28	21.48	1.69	0.89	0.07	12.34	1.19	7.96	0.62	0.18	0.04	0.05	0.01	101.01
	oliv	7	38.23	0.17	0.17	0.02	0.08	0.02	0.27	0.02	20.04	0.14	0.61	0.03	41.51	0.20	0.24	0.01					101.16
	opx	7	54.44	0.14	0.91	0.04	2.20	0.12	0.96	0.03	12.00	0.14	0.58	0.01	28.18	0.24	1.65	0.08	0.03	0.02	0.00	0.01	100.96
C663	liq	14	34.77	1.49	16.94	1.37	4.76	0.21	0.59	0.13	20.40	0.94	0.91	0.04	12.31	1.38	9.08	0.44	0.25	0.06	0.05	0.01	100.06
	oliv	24	38.84	0.11	0.09	0.02	0.08	0.01	0.18	0.02	18.50	0.10	0.62	0.02	42.56	0.26	0.19	0.01					101.06
	opx	10	54.32	0.35	0.81	0.09	2.10	0.16	0.91	0.05	11.44	0.23	0.57	0.01	28.75	0.31	1.47	0.10	0.02	0.02	0.00	0.00	100.41
	spin	5	0.36	0.13	12.07	0.19	11.57	0.54	33.08	0.41	29.46	0.45	0.73	0.02	11.84	0.77	0.06	0.03	0.02	0.02	0.02	0.01	99.20
D414	liq	10	36.00	0.38	15.09	0.32	5.21	0.06	0.84	0.09	20.72	0.25	0.38	0.02	13.04	0.10	7.27	0.14	0.18	0.06	0.04	0.01	98.77
	oliv	10	38.48	0.24	0.13	0.03	0.08	0.01	0.35	0.04	19.25	0.16	0.61	0.03	40.96	0.17	0.20	0.02					100.06
	opx	11	54.09	0.25	0.92	0.04	1.46	0.04	0.88	0.03	11.49	0.18	0.45	0.14	28.82	0.51	1.19	0.04	0.01	0.01	0.00	0.00	99.31
D416	liq	5	39.91	3.98	14.84	1.93	5.03	0.26	0.57	0.17	19.02	1.08	0.74	0.21	10.16	2.15	8.46	0.92	0.13	0.04	0.03	0.01	98.88
	oliv	7	38.38	0.27	0.18	0.03	0.08	0.01	0.28	0.03	20.09	0.16	0.62	0.03	40.10	0.64	0.24	0.01					99.99
	opx	19	52.58	0.47	1.04	0.05	2.11	0.11	0.92	0.05	11.94	0.12	0.44	0.16	28.27	0.45	1.69	0.05	0.03	0.02	0.00	0.00	99.04
	spin	6	0.38	0.14	13.60	0.07	11.05	0.26	33.73	0.30	28.52	0.47	0.69	0.01	11.48	0.46	0.09	0.02	0.00	0.00	0.02	0.00	99.57

Table 6

Electron microprobe analyses of VLTCum1 experiments in oxide weight percents and their 1-σ errors from replicate analyses.

Run	Phase	n	SiO_2	1-σ	TiO_2	1-σ	Al_2O_3	1-σ	Cr_2O_3	1-σ	FeO	1-σ	MnO	1-σ	MgO	1-σ	CaO	1-σ	Na_2O	1-σ	K_2O	1-σ	Total
C666	liq	13	44.87	0.42	0.58	0.02	9.88	0.13	0.33	0.02	17.51	0.24	0.27	0.02	14.80	0.55	11.05	0.31	0.08	0.01	0.11	0.04	99.49

	oliv	10	39.37	1.51	0.00	0.01	0.22	0.30	0.22	0.06	17.72	0.73	0.22	0.01	41.42	1.49	0.50	0.29					99.67
	opx	12	54.06	0.31	0.01	0.01	3.15	0.26	0.72	0.06	10.82	0.08	0.19	0.01	28.00	0.29	2.61	0.04	0.00	0.00	0.01	0.01	99.59
	pig	23	52.70	0.69	0.08	0.02	3.60	0.25	0.64	0.04	10.93	0.23	0.21	0.01	25.70	0.55	5.62	0.44	0.01	0.01	0.02	0.02	99.52
C665	liq	13	46.47	0.19	0.45	0.02	9.52	0.06	0.39	0.03	15.61	0.08	0.29	0.02	15.35	0.12	10.98	0.10	0.06	0.01	0.22	0.04	99.33
	opx	12	54.71	0.35	0.04	0.01	2.32	0.26	0.70	0.05	9.75	0.08	0.19	0.01	29.40	0.29	2.18	0.08	0.00	0.00	0.01	0.01	99.31
C667	liq	12	46.25	0.12	0.44	0.02	9.06	0.08	0.44	0.03	16.57	0.19	0.27	0.01	15.93	0.25	10.45	0.21	0.09	0.04	0.05	0.01	99.54
	oliv	9	39.04	0.27	0.00	0.00	0.10	0.01	0.24	0.03	16.58	0.11	0.22	0.02	43.23	0.35	0.35	0.02					99.76
	opx	13	54.85	0.34	0.03	0.01	2.38	0.16	0.71	0.05	9.87	0.04	0.20	0.01	29.85	0.22	2.05	0.05	0.03	0.02	0.00	0.00	99.96

3. Experimental Results

3.1 Approach to equilibrium and iron loss/gain

To determine whether experiments reached equilibrium, the mineral-melt Fe-Mg exchange coefficient (K_D^{Fe-Mg}) was calculated for each experiment (where K_D^{Fe-Mg} = (X_{Fe}^{xtal} × X_{Mg}^{liq}) / (X_{Mg}^{xtal} × X_{Fe}^{liq})) (Table 3). For the HiTi1 experiments, olivine-melt K_D^{Fe-Mg} values vary from 0.25 to 0.32 with an average value of 0.28. Orthopyroxene-melt K_D^{Fe-Mg} values vary from 0.23 to 0.28 with an average value of 0.24. VLTCum1 experiments have olivine-melt K_D^{Fe-Mg} values between 0.36 and 0.37 with an average of 0.365 and orthopyroxene-melt K_D^{Fe-Mg} values between 0.32 and 0.33 with an average of 0.325. The K_D^{Fe-Mg}'s calculated from these experiments are within the range of K_D^{Fe-Mg}'s reported in previous experimental studies on lunar ultramafic compositions (Wagner and Grove, 1997; Xirouchakis et al, 2001; Krawczynski and Grove, 2012; Brown and Grove, 2015; Guenther, 2021).

In addition to the checks on equilibrium partitioning of Fe and Mg, to ensure a closed system, the phase proportions of minerals and glass and oxide loss/gain for each experiment were calculated using multiple linear regression. For experiments with several phases, this technique is sometimes unsuccessful as it can produce negative phase proportions for some of the minerals. In those instances, the LIME regression technique of Krawczynski and Olive (2011) was utilized. The Fe loss/gain was less than 7.5% for all of the eight HiTi1 and three VLTCum1 experiments.

3.2 HiTi1 experiments

The experimental data for HiTi1 experiments is depicted graphically in Figure 4. Eight experiments span a pressure range of 1.5-2.55 GPa and a temperature range of 1380-1500 °C. Liquid is present in all experiments, and olivine and orthopyroxene co-crystallize in all experiments. Lower temperature experiments at pressures of 1.5 and 2.0 GPa include Cr-rich spinel (Cr_2O_3 > 33 wt.%) as a crystalline phase in addition to melt (Figure 3a). Above 1390°C at 1.5 GPa and 1440°C at 2.0 GPa Cr-spinel leaves the crystalline assemblage.

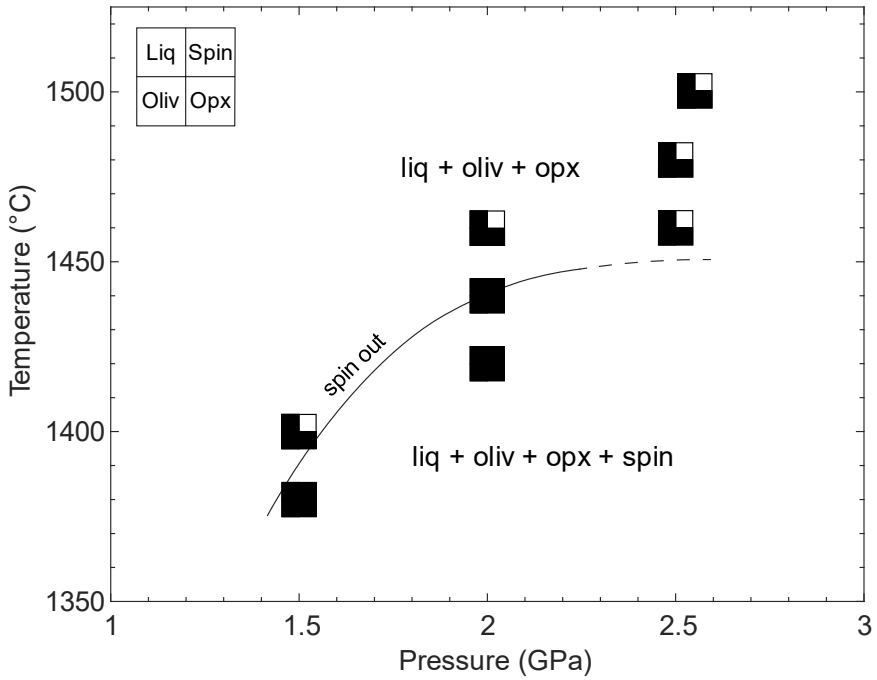

Figure 4. Pressure-temperature grid of HiTi1 experiments performed in this study with symbols indicating the phases produced.

Experimental liquid major oxide compositions are plotting against wt. % MgO in Figure 6 with the target A14B primary magma composition for comparison. MgO contents are within ±2.5 wt. % for all but one experiment. Titanium contents are close to the target composition (Figure 6b), with six out of 8 experiments melts having TiO_2 contents within

±1wt.% of A14B. HiTi1 FeO contents are overall lower than the A14B target (Figure 6c), which Al_2O_3 and CaO were overall higher (Figure 6d, e).

Experimental pressure is also depicted in Figure 6. Calculated Aitchison distances between the experimental melts and the A14B target indicate the best matching experimental compositions are those performed at lower pressures. D414 (1.5 GPa), C651 (1.5 GPa), and C655 (2.0 GPa) are the best matches to A14B, respectively.

3.3 VLTCum1 experiments

The experimental data for VLTCum1 experiments is shown in Figure 5. Three experiments span a pressure range of 1.8-2.0 GPa and 1460-1480°C. Liquid and orthopyroxene are present in all experiments. Between 1.8 and 1.9 GPa at 1480°C olivine is removed as a liquidus phase. The lower temperature, higher pressure experiment at 2.0 GPa and 1460°C includes pigeonite as a crystalline phase in addition to olivine and orthopyroxene (Figure 3b).

VLTCum1 experimental liquid major oxide compositions are plotting against wt. % MgO in Figure 7 with the target A14VLT erupted magma composition for comparison. Experimental liquid MgO contents are within ±0.7 wt. % of A14VLT MgO for all experiments (Figure 7). SiO_2, FeO, and Al_2O_3 contents (wt. %) are also close matches to the target composition (Figure 7a, c, d), having mean percent errors of 1.6%, 2.9%, and 8.9%, respectively. CaO contents plot above A14VLT in all experiments by 1-2 wt. %. TiO_2 contents plot below A14VLT in all experiments, and by ~0.15 wt. % in two of three experiments.

The best matching VLTCum1 experimental melt composition to the A14VLT glass according to Aitchison distance (Eq. 2) is C667 (1.8 GPa), followed by C665 (1.9 GPa), and C666 (2.0 GPa).

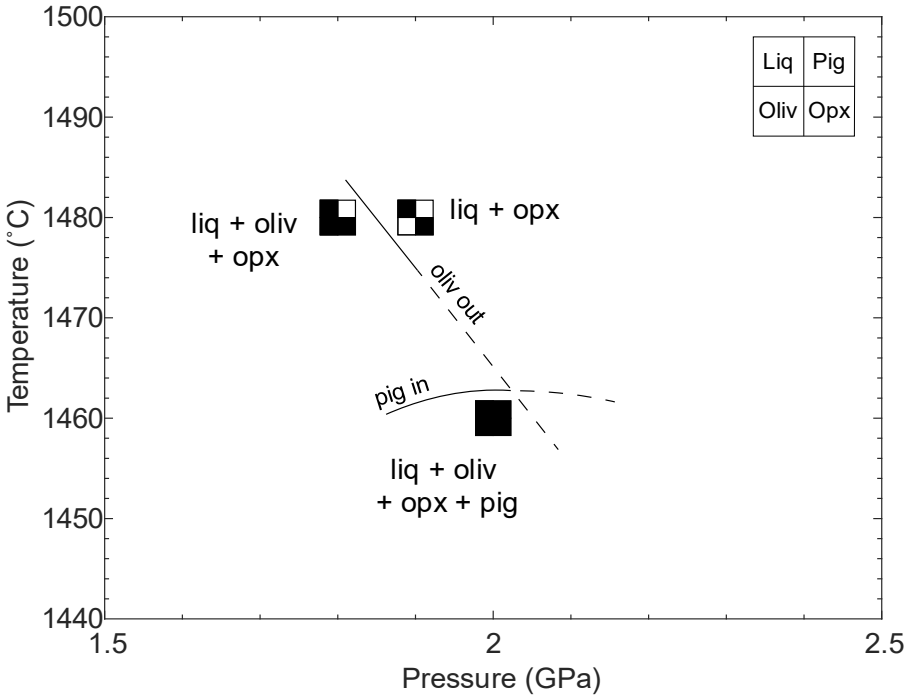

Figure 5. Pressure-temperature grid of VLTCum1 experiments performed in this study with symbols indicating the phases produced.

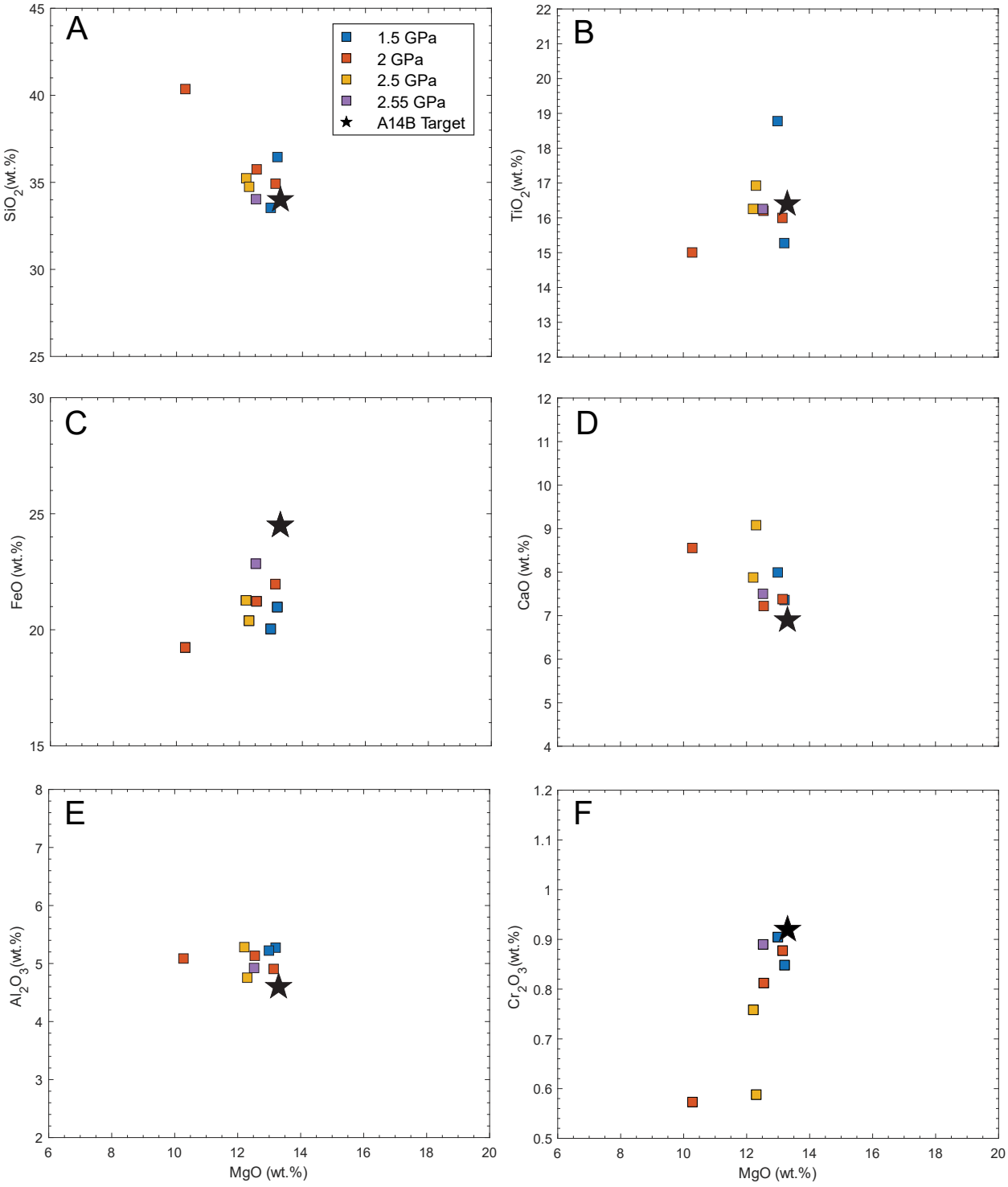

Figure 6. Compositional variation diagrams for the HiTi1 experimental liquids compared to A14B target composition showing major element oxides in wt. % versus MgO in wt. %. Colors correspond to experimental pressures.

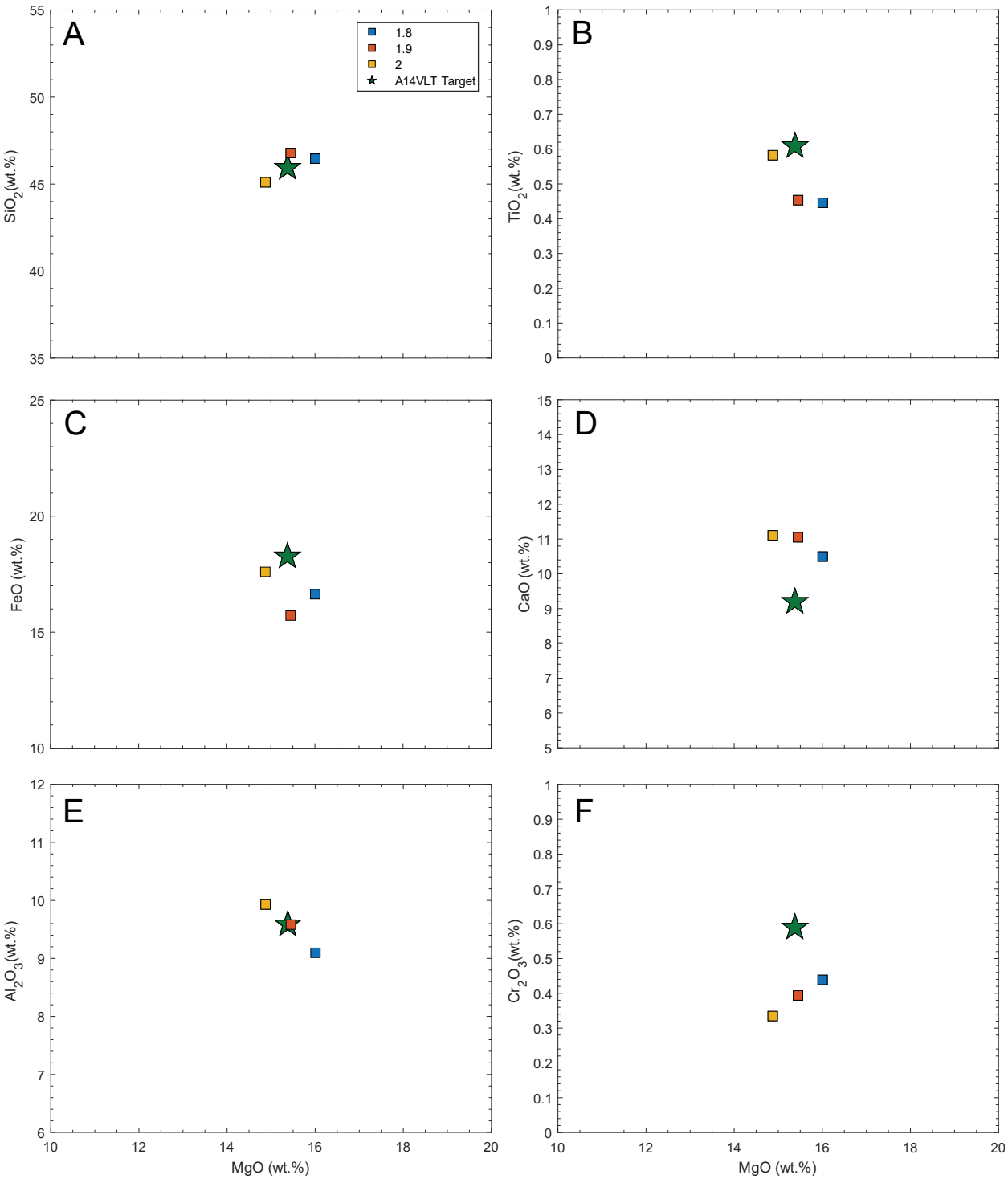

Figure 7. Compositional variation diagrams for the VLTCum1 experimental liquids compared to A14VLT target composition showing major element oxides in wt. % versus MgO in wt. %. Colors correspond to experimental pressures.

4. Discussion

Forward melting experiments on the HiTi1 and VLTCum1 bulk compositions produce melts that plot in the corresponding compositional regions of the lunar ultramafic high- and very low-titanium glasses (Figure 8). Additionally, the pressures, temperatures, and residual mineral assemblages at which the experimental liquids most closely match their target erupted melt compositions correspond to the conditions of multiple saturation and residual phases from previous experimental studies on the A14B and A14VLT glasses (Chen et al., 1982; and Wagner and Grove, 1997; Guenther, 2021).

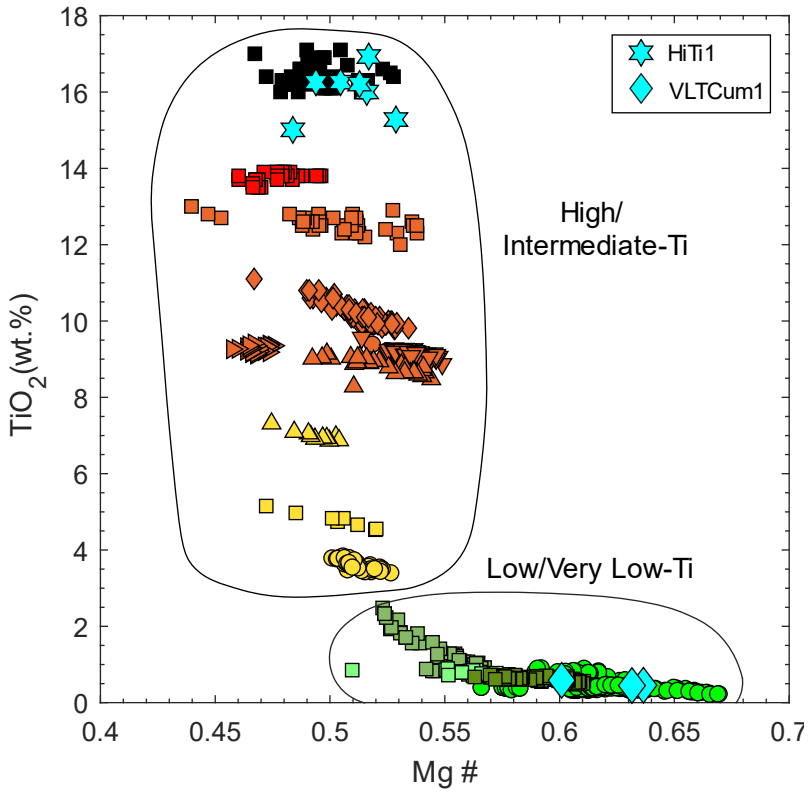

Figure 8. Melts produced in HiTi1 and VLTCum1 experiments overlain on lunar ultramafic glasses. Markers and colors correspond to the same glass suites as in Figure 1. HiTi1 melts plot in the high-Ti compositional region, and VLTCum1 melts are within the low-Ti and VLT space.

4.1 Relationship between multiple saturation point and depth of melting

The three HiTi1 experimental liquids that are the best matches to A14B were produced at pressures of 1.5-2.0 GPa and 1380-1460°C. The residual crystalline phases produced in these experiments include olivine and orthopyroxene for all three experiments, and two (D414, C651) also contain Cr-spinel. Phase equilibrium experiments performed by Wagner and Grove (1997) and Guenther (2021) determined that the A14B composition is multiply saturated with olivine, orthopyroxene, and Cr-spinel at pressures of 1.3-2.1 GPa and temperatures of 1400-1440°C. Thus, there is reasonable overlap between the experimentally produced HiTi1 liquids and their predicted depth and temperature of melting from the A14B source region.

The VLTCum1 liquid composition that most closely resembles the target A14VLT composition was produced at 1.8 GPa and 1480°C, followed by the compositions produced by experiments at 1.9 and 1460°C and 2.0 and 1480°C, respectively. Chen et al. (1982) determined the phase relations of the A14VLT composition. They found an olivine-orthopyroxene multiple saturation point at 1.9 ± 0.1 GPa and 1500 ± 10°C. Olivine was the sole liquidus phase at pressures below the MSP, and orthopyroxene was the sole liquidus phase at pressure above the MSP. The best fitting VLTCum1 liquid had the same crystalline residual phases as A14VLT and was produced under conditions within the predicted multiple saturation pressure range and just below the multiple saturation temperature.

If the HiTi1 and VLTCum1 bulk compositions correspond to the source compositions of their corresponding erupted glass compositions, then the results from both sets of experiments support the multiple saturation hypothesis—that the pressure and

temperature of multiple saturation obtained from inverse melting experiments on the erupted composition corresponds to the conditions experienced by the primary magma at the depth of melting.

4.2 HiTi1 as a source composition of the high-Ti glasses

HiTi1 produces melts with high-TiO_2 contents (>14 wt. %) that closely resemble those found in the A14B suite (Figure 8). The best fitting experimental melts also have CaO contents that are only slightly higher than A14B. This is a clear improvement from previous attempts to produce high-Ti liquids (Van Orman and Grove, 2000; Singletary and Grove, 2008), which were unable to achieve melts with TiO_2 contents over 10 wt. % and CaO contents that coincided with the lunar glass trend.

While FeO contents in HiTi1 melts are lower than expected for A14B, a slightly different source composition could remedy this and other deviations from the target composition. The major challenge in calculating a source composition using Equation (1) is that the D utilized for each component is not well constrained. This is due to the lack of certainty in the olivine:orthopyroxene ratio, which influences the D. For the A14B glass in particular, the composition is multiply saturated with olivine over a range of ~0.8 GPa (Wagner and Grove, 1997; Guenther, 2021). Over that range, the ol:opx ratio would transition between 100:0 and 0:100. Considering the precision in experimental pressure, however, the ratio expressed in multiply saturated experiments may not express the true ol:opx ratio in the source. We found that the testing different ratios during calculations could adjust the calculated bulk composition enough to potentially produce the appropriate compositions in the melts.

Drawing on the results and suggestions of previous studies (Van Orman and Grove, 2000; Kommescher et al., 2020; Brown et al., 2021) and our own findings in this study, we conclude that the high-Ti primary magmas of the high-Ti lunar glasses must have been produced through hybridization invoked through overturn of gravitationally unstable LMO cumulates, rather than through polybaric magma mixing or shallow assimilation of Ti-rich cumulates. Our experimental results confirm that the primary magmas of the high-Ti glasses can be produced by a hybridized mantle source. A hybrid source composition such as HiTi1 can produce the highest-Ti A14B glasses, while a slightly different hybridized source composition such as MOCH (Table 2), which is more enriched in CaO and depleted in TiO_2 and MgO, can produce melts that closely resemble the low-Ti A17O glass.

4.2.1 Origin of the hybridized HiTi1 source region

How are the hybridized source regions of the high-Ti primary magma group produced? Using our simple petrogenetic model, we attempt to determine which end-member components could hybridized to produce the HiTi1 composition, and in what proportions. Previous studies have recognized a requirement for 3 cumulate components to produce the source of the high-Ti magmas. These include a deep ultramafic component, a high-Ti component, a KREEP component (Singletary and Grove, 2008; Brown and Grove, 2015). We test our model with bulk compositions from existing models and experiments that fit these three criteria.

We first test a model with two LMO cumulate components and one KREEP component. We find that it is possible to reasonably reproduce the bulk composition of HiTi1 with ~53% of an ultramafic cumulate, ~32% very late stage pigeonite-augite-

plagioclase-silica-ilmenite cumulate, and ~15% urKREEP, by mass. The best fitting calculations have RMSE < 0.40.

Though the high density of the Ti- and Fe-rich late stage cumulates and overall density stratification of LMO cumulates would impose the gravitational instability required to initiate overturn, viscosity and temperature constraints must be considered to assess whether high-Ti material could have descended to the appropriate depths and within the appropriate time frame for lunar mantle overturn to serve as a viable mechanism for generating the source regions of the high-Ti ultramafic glasses.

Van Orman and Grove (2000) found that temperatures must be low and close to the solidus of ilmenite+pyroxene cumulates (1125°C at 100km depth) in order for those cumulates to be negatively buoyant relative to the underlying ultramafic mantle cumulates. However, at those low temperatures, viscosity of the high-Ti cumulates is high and presents a challenge for reaching the depths inferred for the sources of the high-Ti ultramafic glasses in the time frame required by the onset of high-Ti lunar volcanism. This also calls into question the feasibility of our first model, as it assumes the composition of solid high-Ti cumulates for mass balance calculations.

Van Orman and Grove (2000) suggest an alternative model: physical mixing and chemical reaction of high-Ti liquids and mafic cumulates at shallow depths, which would create a solid hybrid material with a higher solidus temperature and significantly lower viscosity that would sink as diapiers. Investigating this scenario, Elkins-Tanton et al. (2002) calculated that the solidus temperature of the hybrid material would be ~115°C higher than the pure ilmenite+pyroxene cumulate (1240°C at 100 km depth). This could allow the large-scale transport of high-Ti material to occur much more easily than with

pure ilmenite-pyroxene cumulates. Notably, the bulk-composition of this hybrid phase would change the liquidus relations such that spinel would become the titaniferous phase rather than ilmenite (Elkins-Tanton et al., 2002). This is significant because in both this study (HiTi1 experiments) and previous studies on high-Ti liquids (A14B (Wagner and Grove, 1997; Guenther, 2021)) spinel is the liquidus phase found with olivine + orthopyroxene, not ilmenite. This could provide a reasonable alternative to our original model.

Elkins-Tanton et al. (2002) also found another feasible scenario: that the dense liquids produced by high-Ti cumulate remelts could percolate downwards into the lunar mantle and hybridize with the surrounding mantle depth to produce the source regions of the high-Ti magmas. We test this with our model using remelts of high-Ti cumulates instead of solid Ti-cumulates. We find successful calculations with RMSE < 1 for combinations of ~55% early olivine cumulate (38-52% LMO crystallization), ~33-35% remelt of a late stage ilmenite-bearing cumulate, and 11-13% urKREEP. As it descends, the high-Ti liquid would begin to crystallize ilmenite and pyroxene and dissolve olivine, hybridizing the lunar mantle at depths up to 300 km (Elkins-Tanton et al., 2002). Elkins-Tanton et al. (2002) also suggests that this mechanism and the previously mentioned model of Van Orman and Grove (2000) may have both occurred to create a lunar mantle with varying Ti content at depths shallower than 560 km.

4.3 VLTCum1 as a source composition of the high-Al primary magmas

The TiO_2 and Al_2O_3 contents of the VLTCum1 melts are a good match to those displayed by the A14VLT suite (Figure 8, 9). CaO contents, however, are too high in these melts relative to the compositional trend displayed by the VLT glasses (Figure 9).

Notably, the degree of melting observed in the VLTCum1 experiments is significantly higher than expected, with two of the three experiments having and F >40% (Table 4). This is a generally unrealistic degree of melting given the expected thermal conditions of the lunar interior. Lower amounts of CaO are expected for lower degree melts. Further experiments are necessary to better constrain melt compositions produced under more reasonable degrees of melting. Nevertheless, the VLTCum1 composition provides a good approximation of a source for the A14VLT primary magma.

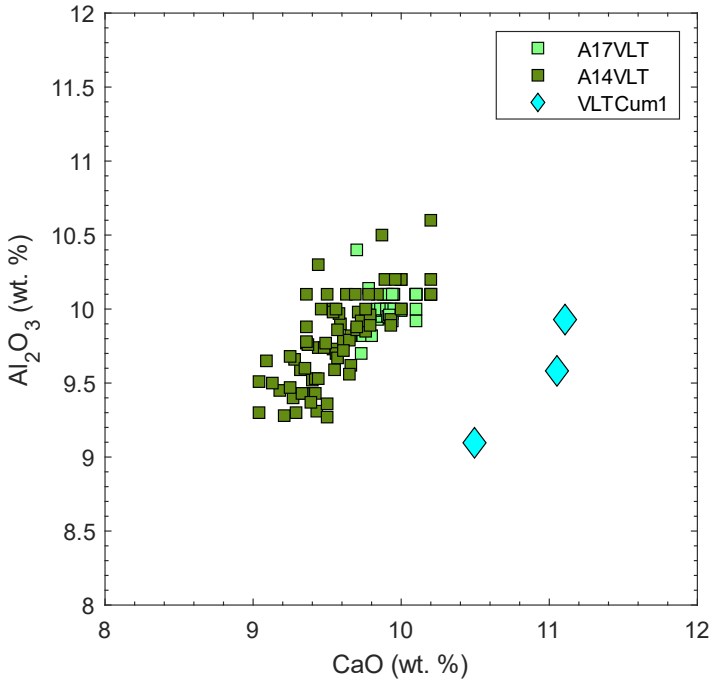

Figure 9. Al_2O_3 vs. CaO. Experimental liquids produced with the VLTCum1 starting material plotting along with the VLT glass data of Delano (1986).

4.3.1 Origin of the VLTCum1 source region

Early study of the VLT glasses (A14 and A17) suggested that these magmas were primary and originated from a pristine cumulate source comprised of olivine and low-Ca pyroxene at depths of 360-380 km within the lunar mantle (Chen et al., 1982). We check this by comparing the VLTCum1 bulk composition to modeled pristine LMO cumulate compositions from Charlier et al. (2018). We find that VLTCum1 does not closely resemble any pristine cumulate composition—all the error calculations have an RMSE > 1.3. This is unsurprising given that VLTCum1 is significantly enriched in Al_2O_3 and CaO relative to a pristine olivine + orthopyroxene cumulate. Thus, we suggest that the A14VLT primary magma is also the product of a heterogeneous mantle source generated through lunar mantle overturn.

To assess this, we test some other potential endmember combinations using our petrogenetic model. We first run our model simply trying combinations of two magma ocean cumulates. With this model, we find moderate success, with only ~100 of the ~6000 tested combinations having RMSE < 1 and the best fitting combinations having RMSE = 0.88. The top fitting combinations were all, by mass, approximately 30% of a late-stage pigeonite-augite-plagioclase cumulate formed at 85% fractional crystallization in the LMO, and approximately 70% of an olivine-orthopyroxene-pigeonite-plagioclase cumulate formed at 80% crystallization.

Our second model tests two cumulate components and one KREEP component, since Apollo 14 glasses display a strong affinity to KREEP (Hughes et al., 1990). This model is more successful at producing source compositions that are a close match to VLTCum1, with ~15000 of ~97700 tested combinations being within the threshold for

success. The dominant trend demonstrated in the lowest error calculations (RMSE < 0.13) is a hybridized source composed of primarily (80%) of an olivine-orthopyroxene-pigeonite-plagioclase cumulate formed at 79% LMO crystallization, a small amount (~6%) of very late stage (95-96% LMO crystallization) pigeonite-augite-plagioclase ± silica cumulate, and a small amount (~13%) of urKREEP (KREEP enriched residual LMO melt) from the last remaining liquid found at 95-99% LMO crystallization. We infer that the urKREEP is retained as an interstitial liquid in the previous cumulate layer as well as the dense, ilmenite-bearing cumulates which are next to crystallize. Gravitational instability brought on by the overlying layers redistributes these three components to greater depths within the lunar mantle, where they re-equilibrate and are later remelted.

Alternatively, it is possible that during LMO crystallization, enough residual melt from the LMO was retained in the cumulate pile to enrich Al_2O_3 and CaO in the source cumulates. Charlier et al. (2018) notes, that 3% interstitial melt is likely the maximum amount of trapped liquid found in the cumulate. However, we still find it unlikely that trapped LMO liquid alone could enrich the lunar mantle in alumina and calcium enough to produce the high-Al primary magmas. Interaction with primordial, deep lunar material should also be considered as a possibility. Most LMO models vary from depths of 400-1000km, implying that the moon was likely never a full magma ocean. Thus, unmelted, undifferentiated material would remain beneath the LMO and later LMO cumulate pile.

While most overturn models do not include the primordial mantle, it is also possible that this material was included in full-scale overturn, or that convective upwelling of the primordial, undifferentiated mantle causes it to partially melt and assimilate with the overlying cumulates. The primordial lunar mantle is expected to be a garnet lherzolite and

could be a candidate for supplying Al_2O_3 and CaO for the source region of A14VLT. Along these lines, Barr and Grove (2013) suggested that mixing 80% overturned remelted late-stage cumulate material with 20% primordial lunar mantle melt could produce the Apollo 15 Green A glasses. Although the A14VLT glass is much more Al- and Ca-rich than A15Ga, compositional heterogeneity in the overturned mantle cumulates could allow for these glasses to be produced in similar ways.

Using our petrogenetic model, we test the combination of a melt of primordial lunar mantle (LPUM (Longhi, 2006)) with one and two LMO cumulate components. We find results similar to Barr and Grove (2013), with the best fitting cumulate-LPUM melt combination consisting of 85% late-stage (78-81% LMO crystallization) olivine-orthopyroxene-plagioclase-pigeonite cumulate and 15% LPUM melt (RMSE $\approx$ 0.38). With two cumulates, we find an even better fit (RMSE $\approx$ 0.11) with ~4% an even later-stage cumulate (82-96% LMO crystallization) in addition to the same components from the previous model in the proportions of 83% and 13%, respectively. While this modeling is preliminary and requires more consideration of thermal and trace element constraints, it nevertheless demonstrates that more consideration should be given to the possible participation of primordial lunar mantle in lunar mantle overturn and/or lunar ultramafic glass genesis. In the scenario where an overturned LMO cumulate(s) is mixed with a primordial mantle melt, the multiple saturation pressures/temperatures indicated from experiments represent the depth and thermal conditions at which the overturned cumulates were remelted by upwelling partial melts of the underlying lunar mantle.

4.4 Buoyancy of the ultramafic magmas

The magmas that produced the lunar ultramafic magmas are high-density liquids, especially the high-Ti glasses. Melt buoyancy is one of the primary concerns that has been raised by previous investigators to disqualify remelts of hybridized cumulates as a feasible source for the high-Ti glasses (Circone and Agee, 1996; Wagner and Grove, 1997; Elkins-Tanton et al., 2002). Here we investigate the density of these melts relative to depth within the lunar mantle to assess the validity of these concerns.

4.4.1 Buoyancy of the high-Ti magmas

We first calculate the depth-density curves of a selection of high-Ti glasses using the methods of Delano (1990). This entails performing iterative calculations to solve for the high-pressure density of the liquids using a third-order Birch-Murnaghan equation of state:

$$P = \frac{3}{2} \cdot K_T^{\circ} \cdot \left[\left(\frac{\rho}{\rho_{\circ}}\right)^{\frac{7}{3}} - \left(\frac{\rho}{\rho_{\circ}}\right)^{\frac{5}{3}} \right] \cdot \left[1 - \frac{3}{4} \cdot (4 - K_T') \cdot \left[\left(\frac{\rho}{\rho_{\circ}}\right)^{\frac{2}{3}} - 1 \right] \right] \qquad (3)$$

where P = pressure in GPa; K_T° = isothermal bulk modulus (GPa) of the liquid at 1-atm pressure and temperature, T; $\rho_{\circ}$ = density of the liquid at 1-atm pressure and temperature, T; ρ = density of the liquid at high pressure, P and temperature, T; K_T' = pressure derivative of the isothermal bulk modulus. We use the compositional parameters of Lange and Carmichael (1987), and we assume an intermediate value of 6 for K_T' (Delano, 1990; Krawczynski and Grove, 2012).

Calculated density profiles for three high-Ti glasses, Apollo 17 Orange, Apollo 15 Red, and Apollo 14 Black, are shown in Figure 10. We compare these profiles to the density profile of the differentiated (post-overturn) lunar mantle density profile from Hess and

Parmentier (1995). This provides an approximate comparison of the high-Ti magmas relative to their solid mantle residue.

Also indicated in Figure 10 are the pressure ranges of multiple saturation from phase equilibrium experiments on these glass compositions (Wagner and Grove, 1997; Krawczynski and Grove 2012; Guenther, 2021). The high-Ti glasses are multiply saturated over a range of pressures depending on the oxygen fugacity (f_{O_2}) conditions experienced in their source regions. More oxidizing experimental f_{O_2} conditions (IW + 1.5) indicate shallower depths of melting, while more reducing conditions (IW – 2.1) push the depths of melting further into the lunar interior. The magnitude of the difference in melting depths under these varying conditions is directly related to TiO_2 content in the liquids (Guenther, 2021).

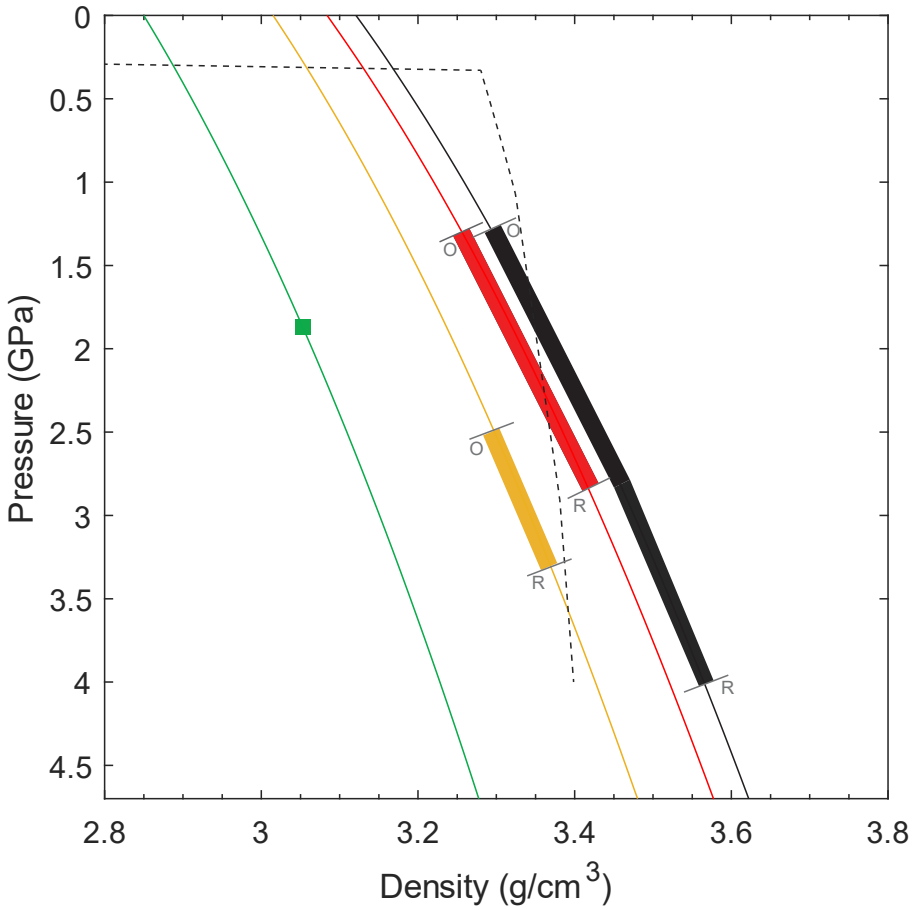

Figure 10. Calculated liquid density depth curves for the A14VLT (green line), A17O (orange line), A15R (red line), and A14B (black line) shown relative to a model density profile (dashed line) of the post-overturn lunar mantle (Hess and Parmentier, 1995). The ranges of MSP for the high-titanium glasses are shown as thick bars and the experimental f_{O_2} conditions are shown at their respective depths with dark gray lines and markers O (IW + 1.5) and R (IW – 2.1), indicating oxidizing and reducing conditions, respectively.

In order to be positively buoyant and segregate from their mantle residues, the high-Ti magmas must have melted at pressures that correspond with densities lower than that of the surrounding lunar mantle. While it is evident that the A17O liquid is buoyant over its entire range of experimentally determined multiple saturation pressures (2.5-3.3 GPa), the higher-Ti A15R and A14B glasses are only positively buoyant at pressures which correspond to more oxidizing f_{O_2} conditions—less than 1.7 GPa for A14B and ~2.3 GPa

for A15R (Figure 10). We suggest, in agreement with Guenther (2021), that the source regions of these magmas are more oxidizing (IW > 0) than previous estimates (IW < 0).

4.4.2 Buoyancy of the A14VLT magma

The density profile of the low-Ti, A14VLT magma in the lunar mantle is also included in Figure 10. This liquid is always buoyant relative to the Hess and Parmentier (1995) differentiated lunar mantle. Therefore, we expect that there would be no issue in its buoyant ascent from its depth of melting (~1.9 GPa) within the lunar mantle.

4.4.3 Precise considerations of mantle residue density at depth

While the differentiated mantle density profile of Hess and Parmentier (1995) provides a useful visualization of density stratification in an overturned lunar mantle, it is not a definitive quantitative constraint on post-overturn lunar mantle density, which is likely laterally heterogeneous given the similar range multiple saturation depths of both the high- and low-Ti ultramafic glasses. Vanderkaaden et al. (2015) conducted a different technique for comparing the densities of these liquids relative to their mantle resides. They calculated the density of the equilibrium residual mantle minerals (olivine + orthopyroxene) specifically at the average depth of melting using information provided by multiple saturation experiments on the ultramafic glasses. Since it is difficult to place constraints on the olivine-orthopyroxene ratio of the mantle from experiments alone, they used the Birch-Murnaghan equation of state (Equation (3)) to calculate the pressure dependent density curves of the equilibrium olivine and orthopyroxene and compare both to the glass density

curve. This provides a range of possible mantle source region densities and brackets the pressures at which a density crossover would occur.

Vanderkaaden et al. (2015) determined that the A14B melt could ascend through the lunar mantle by buoyancy forces alone as long as the surrounding mantle was comprised of ≤87% pyroxene. They suggest that likely mineral proportions in the lunar mantle favor the buoyant ascent of A14B. The mineral proportions suggested by our model and proportions of multiply saturated minerals from previous experiments (Wagner and Grove, 1997; Guenther, 2021) also confirm this suggestion. The point at which the black glass becomes negatively buoyant according to their calculations is at ~2.2 GPa. This is slightly deeper than what is suggested by our approach (Figure 10) but would also correspond with a source region comprised of nearly 100% olivine, which is unlikely. It is clear with either approach, the melting depths associated with low oxidation conditions are negatively buoyant. Therefore, we hold that more oxidizing source conditions are a requirement for at least the highest-Ti magmas.

Vanderkaaden et al. (2015) did not calculate the density curve of the A14VLT glass specifically, but they did do calculations for another, similar density low-Ti glass, the Apollo 15 Green C. In accordance with our density comparison, they found that liquid to be buoyant far beyond its suggested depth of melting.

5. Conclusions

We have investigated the source regions of the high-Ti and high-Al primary magmas. Forward melting experiments on HiTi1, a calculated hybrid source composition for the highest titanium glass suite, A14B, confirm that the source of the high-Ti primary magma is derived through hybridization of LMO cumulates instigated by lunar mantle overturn. Our petrogenic model suggests a hybrid source comprised of (1) an early ultramafic LMO cumulate, (2) a late-stage, high-Ti cumulate, or high-Ti cumulate remelt, and (3) a KREEP component.

The high-Al, low-Ti primary magma which produced the A14VLT glass suite cannot be derived from an early mafic cumulate source alone. Our calculated source composition, VLTCum1, provides insight into the possible components that could be involved in producing the source region of the VLT glasses. Our petrogenetic calculations suggests a hybrid source comprised of (1) two late stage cumulate components + a KREEP component or (2) two late stage cumulate components + a partial melt of the undifferentiated lunar mantle below the LMO are the best fitting models for generating a VLTCum1 source. However, further experimentation on modified source compositions may provide more insight.

Our experiments produced liquids that are a close match to target erupted compositions, and the crystalline phases present match the residual phases noted in previous studies on the ultramafic glasses. This suggests that the multiple saturation pressures and temperatures determined for the ultramafic glasses can serve as an indicator of the depth and temperature within the lunar mantle of melting for a buoyant primary magma.

References

Aitchison, J., Barceló-Vidal, C., Martín-Fernández, J. A., & Pawlowsky-Glahn, V. (2000). Logratio Analysis and Compositional Distance 1. *Mathematical Geology* (Vol. 32, Issue 3).

Armstrong, J. T. (1995). Citzaf-a package of correction programs for the quantitative Electron Microbeam X-Ray-Analysis of thick polished materials, thin-films, and particles. *Microbeam Analysis*, *4*(3), 177–200.

Barr, J. A., & Grove, T. L. (2013). Experimental petrology of the Apollo 15 group A green glasses: Melting primordial lunar mantle and magma ocean cumulate assimilation. *Geochimica et Cosmochimica Acta*, *106*. https://doi.org/10.1016/j.gca.2012.12.035

Boyd, F. R., & England, J. L. (1960a). *Apparatus for Phase-Equilibrium Measurements at Pressures up to 50 Kilobars and Temperatures up to 1750C* (Vol. 65, Issue 2).

Boyd, F. R., & England, J. L. (1960b). Apparatus for phase-equilibrium measurements at pressures up to 50 kilobars and temperatures up to 1750°C. *Journal of Geophysical Research*, *65*(2), 741–748. https://doi.org/10.1029/JZ065I002P00741

Brodsky, H. F., Brown, S. M., & Grove, T. L. (2019). Origin of the high-titanium lunar glasses: Constraints from cumulate remelting experiments. *50th Lunar and Planet. Sci. Conf.* , *#2132*.

Brown, S. M., & Grove, T. L. (2015). Origin of the Apollo 14, 15, and 17 yellow ultramafic glasses by mixing of deep cumulate remelts. *Geochimica et Cosmochimica Acta*, *171*, 201–215. https://doi.org/10.1016/j.gca.2015.09.001

Brown, S. M., & Grove, T. L. (2017). Mixing of melts of compositionally distinct source regions can explain the within- and between-suite compositional variability of the lunar ultramafic glasses: experiments and models. *48th Lunar Planet. Sci. Conf.* , *#2176*.

Charlier, B., Grove, T. L., Namur, O., & Holtz, F. (2018). Crystallization of the lunar magma ocean and the primordial mantle-crust differentiation of the Moon. *Geochimica et Cosmochimica Acta*, *234*, 50–69. https://doi.org/10.1016/j.gca.2018.05.006

Chen, H. K., Delano, J. W., & Lindsley, D. H. (1982). Chemistry and phase relations of VLT volcanic glasses from Apollo 14 and Apollo 17. *Journal of Geophysical Research*, *87*(Supplement). https://doi.org/10.1029/jb087is01p0a171

Circone, S., & Agee, C. B. (1996). Compressibility of molten high-Ti mare glass: Evidence for crystal-liquid density inversions in the lunar mantle. *Geochimica et Cosmochimica Acta*, *60*(14), 2709–2720. https://doi.org/10.1016/0016-7037(96)00117-2

Delano, J. W. (1986a). Pristine lunar glasses: Criteria, data, and implications. *Journal of Geophysical Research: Solid Earth*, *91*(B4), 201–213. https://doi.org/10.1029/jb091ib04p0d201

Delano, J. W. (1990). Buoyancy-driven melt segregation in Earth's Moon, I. Numberical Results. *Proc. Lunar Planet. Sci. Conf. 20th*, 3–12.

Elardo, S. M., Draper, D. S., Shearer, C. K. , Jr., Elardo, S. M., Draper, D. S., & Shearer, C. K. , Jr. (2011). Lunar Magma Ocean crystallization revisited: Bulk composition, early cumulate mineralogy, and the source regions of the highlands Mg-suite. *GeCoA*, *75*(11), 3024–3045. https://doi.org/10.1016/J.GCA.2011.02.033

Elkins Tanton, L. T., van Orman, J. A., Hager, B. H., & Grove, T. L. (2002). Re-examination of the lunar magma ocean cumulate overturn hypothesis: Melting or mixing is required. *Earth and Planetary Science Letters*, *196*(3–4), 239–249. https://doi.org/10.1016/S0012-821X(01)00613-6

Elkins-Tanton, L. T., Burgess, S., & Yin, Q. Z. (2011). The lunar magma ocean: Reconciling the solidification process with lunar petrology and geochronology. *Earth and Planetary Science Letters*, *304*(3–4), 326–336. https://doi.org/10.1016/J.EPSL.2011.02.004

Elkins-Tanton, L. T., Chatterjee, N., & Grove, T. L. (2003). Experimental and petrological constraints on lunar differentiation from the Apollo 15 green picritic glasses. *Meteoritics & Planetary Science*, *38*(4), 515–527. https://doi.org/10.1111/J.1945-5100.2003.TB00024.X

Guenther, M. E. (2021). *The Influence of Variable Oxygen Fugacity on the Source Depths for Lunar High-Titanium Ultramafic Glasses* [B.S.]. Massachusetts Institute of Technology.

Hays, J. F. (1966a). Lime-alumina-silica. *Carnegie Institute of Washington Yearbook*, *65*, 234–289.

Hays, J. F. (1966b). Stability and properties of the synthetic pyroxene CaAl2SiO6. *American Mineralogist*, *51*(9), 1524–1529.

Herbert, F. (1980). Time dependent lunar density models. *Proc. Lunar Planet. Sci. Conf. 11*, 2015–2030.

Hess, P. C., & Parmentier, E. M. (1995). A model for the thermal and chemical evolution of the Moon's interior: implications for the onset of mare volcanism. *Earth and Planetary Science Letters*, *134*(3–4), 501–514. https://doi.org/10.1016/0012-821X(95)00138-3

Hubbard, N. J., & Minear J. W. (1976). A chemical and physical model for the genesis of lunar rocks: Part II. Mare basalts. . *Proc. Lunar Planet. Sci. Conf.* , *6*, 405–407.

Hughes, S. S., Delano, J. W., & Schmitt, R. A. (1990). Chemistry of individual mare volcanic glasses: evidence for distinct regions of hybridized mantle and a KREEP component in Apollo 14 magmatic sources. *Proc. Lunar Planet. Sci. Conf. 20th*, 127–138.

Kommescher, S., Fonseca, R. O. C., Kurzweil, F., Thiemens, M. M., Münker, C., & Sprung, P. (2020). Unravelling lunar mantle source processes via the Ti isotope composition of lunar basalts. *Geochemical Perspectives Letters*, *13*, 13–18. https://doi.org/10.7185/geochemlet.2007

Krawczynski, M. J., & Grove, T. L. (2011). A new fitting algorithm for petrological mass balance problems. *AGU Fall Meeting Abstracts*, *#2613*.

Krawczynski, M. J., & Grove, T. L. (2012). Experimental investigation of the influence of oxygen fugacity on the source depths for high titanium lunar ultramafic magmas. *Geochimica et Cosmochimica Acta*, *79*, 1–19. https://doi.org/10.1016/j.gca.2011.10.043

Krein, S. B., Guenther, M. E., & Grove, T. L. (2021). Source Regions of the Lunar Ultramafic Glasses Constrained by Experiments and Models. *52nd Lunar and Planetary Science Conference*, *#2483*.

Lange, R. A., & Carmichael, I. S. E. (1987). Densities of Na2O-K2O-CaO-MgO-FeO-Fe2O3-Al2O3-TiO2-SiO2 liquids: New measurements and derived partial molar properties. *Geochimica et Cosmochimica Acta*, *51*(11), 2931–2946. https://doi.org/10.1016/0016-7037(87)90368-1

Lin, Y., Tronche, E. J., Steenstra, E. S., & van Westrenen, W. (2017). Experimental constraints on the solidification of a nominally dry lunar magma ocean. *Earth and Planetary Science Letters*, *471*, 104–116. https://doi.org/10.1016/J.EPSL.2017.04.045

Longhi, J. (2005a). Temporal stability and pressure calibration of barium carbonate and talc/pyrex pressure media in a piston-cylinder apparatus. *American Mineralogist*, *90*(1), 206–218.

Longhi, J. (2006). Petrogenesis of picritic mare magmas: Constraints on the extent of early lunar differentiation. *Geochimica et Cosmochimica Acta*, *70*(24), 5919–5934. https://doi.org/10.1016/J.GCA.2006.09.023

Médard, E., McCammon, C. A., Barr, J. A., & Grove, T. L. (2008a). Oxygen fugacity, temperature reproducibility, and H2O contents of nominally anhydrous piston-cylinder experiments using graphite capsules. *American Mineralogist*, *93*(11–12), 1838–1844. https://doi.org/10.2138/AM.2008.2842

Neal, C. R., & Taylor, L. A. (1989). Metasomatic products of the lunar magma ocean: The role of KREEP dissemination. *Geochimica et Cosmochimica Acta*, *53*(2), 529–541. https://doi.org/10.1016/0016-7037(89)90403-1

Parmentier, E. M., Zhong, S., & Zuber, M. T. (2002). Gravitational differentiation due to initial chemical stratification: origin of lunar asymmetry by the creep of dense KREEP? *Earth and Planetary Science Letters*, *201*(3–4), 473–480. https://doi.org/10.1016/S0012-821X(02)00726-4

Philpotts, J. A., & Schnetzler, C. C. (1970). Potassium, Rubidium, Strontium, Barium, and Rare-Earth Concentrations in Lunar Rocks and Separated Phases. *Science*, *167*(3918), 493–495. https://doi.org/10.1126/SCIENCE.167.3918.493

Putirka, K., Johnson, M., Kinzler, R., Longhi, J., & Walker, D. (1996a). Thermobarometry of mafic igneous rocks based on clinopyroxene-liquid equilibria, 0-30 kbar. *Contrib Mineral Petrol*, *123*, 92–108.

Ringwood, A. E., & Kesson, S. E. (1976). A dynamic model for mare basalt petrogenesis. *Proc. Lunar Planet. Sci. Conf. 7*, *2*, 1697–1722.

Schaeffer, O. A., & Husain, L. (1973). Early lunar history: Ages of 2 to 4 mm soil fragments from the lunar highlands. *Proceedings of the Lunar Science Conference*, *4*, 1847.

Shearer, C. K., Hess, P. C., Wieczorek, M. A., Pritchard, M. E., Parmentier, E. M., Borg, L. E., Longhi, J., Elkins-Tanton, L. T., Neal, C. R., Antonenko, I., Canup, R. M., Halliday, A. N., Grove, T. L., Hager, B. H., Lee, D. C., & Wiechert, U. (2006). Thermal and Magmatic Evolution of the Moon. *Reviews in Mineralogy and Geochemistry*, *60*(1), 365–518. https://doi.org/10.2138/RMG.2006.60.4

Shearer, C. K., Papike, J. J., & Layne, G. D. (1996). Deciphering basaltic magmatism on the Moon from the compositional variations in the Apollo 15 very low-Ti picritic magmas. *Geochimica et Cosmochimica Acta*, *60*(3), 509–528. https://doi.org/10.1016/0016-7037(95)00406-8

Singletary, S., & Grove, T. (2008). Origin of lunar high-titanium ultramafic glasses: A hybridized source? *Earth and Planetary Science Letters*, *268*(1–2), 182–189. https://doi.org/10.1016/J.EPSL.2008.01.019

Sio, C. K., Borg, L. E., & Cassata, W. S. (2020). The timing of lunar solidification and mantle overturn recorded in ferroan anorthosite 62237. *Earth and Planetary Science Letters*, *538*, 116219. https://doi.org/10.1016/j.epsl.2020.116219

Smith, J. v., Anderson, A. T., Newton, R. C., Olsen, E. J., Crewe, A. v., & Isaacson, M. S. (1970). Petrologic history of the moon inferred from petrography, mineralogy and petrogenesis of Apollo 11 rocks. *Proceedings of the Apollo 11 Lunar Science Conference*, *1*, 897–926.

Snyder, G. A., Taylor, L. A., & Neal, C. R. (1992). A chemical model for generating the source of mare basalts: Combined equilibrium and fractional crystallization of the lunar magmasphere. *Geochimica et Cosmochimica Acta*, *56*, 3809–3823.

Spangler, R. R., Warasila, R., & Delano, J. W. (1984). Ar-39-Ar-40 ages for the Apollo 15 green and yellow volcanic glasses. *Journal of Geophysical Research*, *89*(S02), B487. https://doi.org/10.1029/JB089iS02p0B487

Taylor, S. R. (1973). Chemical evidence for lunar melting and differentiation. *Nature*, *245*, 203–205.

Taylor, S. R., & Jakes, P. (1974). The geochemical evolution of the moon. *Proceedings of the Fifth Lunar Conference*, *2*, 1287–1305.

van Orman, J. A., & Grove, T. L. (2000). Origin of lunar high-titanium ultramafic glasses: Constraints from phase relations and dissolution kinetics of clinopyroxene-ilmenite cumulates. *Meteoritics & Planetary Science*, *35*(4), 783–794.

vander Kaaden, K. E., Agee, C. B., & McCubbin, F. M. (2015). Density and compressibility of the molten lunar picritic glasses: Implications for the roles of Ti and Fe in the structures of silicate melts. *Geochimica et Cosmochimica Acta*, *149*, 1–20. https://doi.org/10.1016/J.GCA.2014.10.029

Wagner, T. P., & Grove, T. L. (1997). Experimental constraints on the origin of lunar high-Ti ultramafic glasses. *Geochimica et Cosmochimica Acta*, *61*(6), 1315–1327. https://doi.org/10.1016/S0016-7037(96)00387-0

Walker, D., Longhi, J., & Hayes, J. F. (1975). Differentiation of a very thick magma body and implications for the source regions of mare basalts. *Proc. Lunar Sci. Conf.* , *6*, 1103–1120.

Warren, P. H., & Wasson, J. T. (1979). The origin of KREEP. *Reviews of Geophysics*, *17*(1), 73–88. https://doi.org/10.1029/RG017I001P00073

Wood, J. A., Dickey, J. S. J., Marvin, U. B., & Powell, B. N. (1970). Lunar anorthosites and a geophysical model of the moon. *Proceedings of the Apollo 11 Lunar Science Conference*, *1*, 965.

Xirouchakis, D., Hirschmann, M. M., & Simpson, J. A. (2001). The effect of titanium on the silica content and on mineral-liquid partitioning of mantle-equilibrated melts. *Geochimica et Cosmochimica Acta*, *65*(14), 2201–2217. https://doi.org/10.1016/S0016-7037(00)00549-4

Yu, S., Tosi, N., Schwinger, S., Maurice, M., Breuer, D., & Xiao, L. (2019). Overturn of Ilmenite-Bearing Cumulates in a Rheologically Weak Lunar Mantle. *Journal of Geophysical Research: Planets*, *124*(2), 418–436. https://doi.org/10.1029/2018JE005739

Zhao, Y., de Vries, J., van den Berg, A. P., Jacobs, M. H. G., & van Westrenen, W. (2019). The participation of ilmenite-bearing cumulates in lunar mantle overturn. *Earth and Planetary Science Letters*, *511*, 1–11. https://doi.org/10.1016/j.epsl.2019.01.022